

# The numerical investigation of a planar single chamber solid oxide fuel cell performance with a focus on the support types

Kamvar, Majid; Ghassemi, Majid; Steinberger-Wilckens, Robert

DOI:

[10.1016/j.ijhydene.2019.12.220](https://doi.org/10.1016/j.ijhydene.2019.12.220)

License:

None: All rights reserved

*Document Version*

Peer reviewed version

*Citation for published version (Harvard):*

Kamvar, M, Ghassemi, M & Steinberger-Wilckens, R 2020, 'The numerical investigation of a planar single chamber solid oxide fuel cell performance with a focus on the support types', *International Journal of Hydrogen Energy*, vol. 45, no. 11, pp. 7077-7087. <https://doi.org/10.1016/j.ijhydene.2019.12.220>

[Link to publication on Research at Birmingham portal](#)

## General rights

Unless a licence is specified above, all rights (including copyright and moral rights) in this document are retained by the authors and/or the copyright holders. The express permission of the copyright holder must be obtained for any use of this material other than for purposes permitted by law.

- Users may freely distribute the URL that is used to identify this publication.
- Users may download and/or print one copy of the publication from the University of Birmingham research portal for the purpose of private study or non-commercial research.
- User may use extracts from the document in line with the concept of 'fair dealing' under the Copyright, Designs and Patents Act 1988 (?)
- Users may not further distribute the material nor use it for the purposes of commercial gain.

Where a licence is displayed above, please note the terms and conditions of the licence govern your use of this document.

When citing, please reference the published version.

## Take down policy

While the University of Birmingham exercises care and attention in making items available there are rare occasions when an item has been uploaded in error or has been deemed to be commercially or otherwise sensitive.

If you believe that this is the case for this document, please contact [UBIRA@lists.bham.ac.uk](mailto:UBIRA@lists.bham.ac.uk) providing details and we will remove access to the work immediately and investigate.

# The numerical investigation of a planar single chamber solid oxide fuel cell performance with a focus on the support types

Majid Kamvar<sup>a,\*</sup>, Majid Ghassemi<sup>b</sup> and Robert Steinberger-Wilckens<sup>c</sup>

<sup>a</sup>Assistant Professor, Department of Mechanical Engineering, Parand Branch, Islamic Azad University, Parand, Iran

<sup>b</sup>Professor, Department of Mechanical Engineering, K. N. Toosi University of Technology, Tehran, Iran

<sup>c</sup>Professor, Center for Fuel Cell and Hydrogen Research, School of Chemical Engineering, University of Birmingham, Edgbaston, B15 2TT, UK

## Abstract

Single chamber solid oxide fuel cells (SC-SOFCs) could be an alternative to the conventional dual chamber types since they do not need any sealant and electrolyte crack growth does not lead to failure in performance. However, the reduced reactant activity due to spectator species present at anode and cathode results in a significantly decreased performance. The focus of this paper is to present a comparative study on the performance of single-chamber anode-, cathode, and electrolyte-supported cells. Our results show that anode-supported cells offer significantly better performance compared to electrolyte-supported cells. The cathode-supported cells show a similar performance to anode-supported cell close to open circuit voltages, i.e. voltages above 0.92V, after which the cell current density decreases due to lack of oxygen at the cathode catalyst layer. Finally, a time-dependent performance study of the cathode-supported cell concept is presented and discussed.

Keywords: Single chamber, Solid oxide fuel cell, Hydrogen-Air, Premixed, Lack of Oxygen, Support types

## 1. Introduction

Fuel cells are an efficient technology for generating electricity through direct electrochemical conversion of a fuel and an oxidant without thermal conversion [1]. SOFCs are gaining considerable attention due to their high efficiency and the fuel flexibility [2-6]. SOFCs work

---

\* Corresponding author, Tel.: +9821-5673-3037; E-mail: mkamvar@mail.kntu.ac.ir

at high temperatures between 500 and 950°C [7]. These high operating temperatures have both advantages and disadvantages. On one hand they enable direct internal reforming at the anode as well as the fuel flexibility, on the other hand they can lead to crack formation within SOFC components due to thermal stresses [8,9]. Also, the high operating temperature gives rise to increased materials degradation [10-13]. In this respect, single chamber solid oxide fuel cells (SC-SOFC) could be an alternative since they do not need any sealant and any crack growth would not terminate their performance. However, SC-SOFCs suffer from very low performance compared to conventional SOFCs. This low performance is mostly due to the presence of ‘spectator’ species at the two catalyst layers (for example transport of hydrogen to the cathode catalyst layer) which currently reduces their development interest to research projects. Thus, there exists some interest in studying SC-SOFCs and finding pathways to improve their performance and the management of energy transfer.

Studies that have investigated SC-SOFC behavior can be divided into two categories, namely “numerical” and “experimental” approaches. Experimental studies will be factual and represent the ‘real world’ performance of SC-SOFC. However, experimental tests are usually cost intensive, consume time and energy, and are usually unable to provide details including the concentration of chemical species at the electrodes, the velocity of fluid flow or local current densities etc. Nevertheless, knowledge of such data would play a key role in improving cell performance and facilitating device improvement. Accordingly, the development of numerical studies in this area provides very useful details especially as there is too little experimental information on SC-SOFCs performance. Indeed, a number of studies on SC-SOFC have been performed using numerical approaches and published in [2, 10, 13-25]. Among these few numerical models, Chung et al. [14] reported that ohmic loss in comparison to the other two voltage losses (i.e. concentration and activation losses) was the major term present in SC-SOFCs. For this reason, different anode and cathode arrangements

can affect the SC-SOFC performance by changing the path of movement of the oxygen ions from the cathode to the anode and thus influencing the ohmic loss occurring in the cell. Wang et al. [8] presented a novel configuration for SC-SOFC called right-angular configuration. Since their study was limited to experiment, detailed information about the physico-chemistry was not reported. Kamvar et. al. [2] performed a comparison study between different anode and cathode configurations on SC-SOFC. Their results revealed that the ohmic losses play a key role in cell performance improvement. Recently, Xu et. al. [26] developed numerical models for button all porous dual chamber solid oxide fuel cells. Their results focused on electrolyte porosity optimization to control the oxygen transport to the anode to prevent the risk of simple combustion (and explosion) which would considerably reduce the cell performance. However, a number of useful recent numerical studies have been performed on SOFC area. Kong et. al. [26] proposed a novel interconnector design named X-type interconnector. Their numerical results showed that the cell with this novel design presented better performance compared to the cell with conventional interconnector. Schluckner et. al. [27] studied on the influence of different possible flow configurations and electrical contact positions on the temperature distribution within the cell. They claimed that it was not possible to move the maximum cell temperature to the cell centre by a variation of the electrical contact position. Moreno-Blanco et. al. [28] numerically studied on the effect of channels-electrode interface area on the performance of planar SOFC. They found out that the size (width) and number of channels in a co-flow arrangement had a direct effect on the cell performance.

In this study, the evaluation of the performance of a planar single chamber solid oxide fuel cell within a wide range of voltages is our target. The focus is laid on the control of the amount of oxygen present at the cathode functional layer

## **2. Problem Definition**

A 2D numerical model was used to predict the performance of a single planar SC-SOFC. In the planar type of SC-SOFC, the electrolyte is sandwiched between two porous electrodes. As shown in Fig.1, a single cell is located in the middle of a reaction chamber. 50% hydrogen, 50% air by volume is used to ensure the system safety [16]. Using hydrogen as a fuel is a benefit because: i) it avoids coking problems, and ii) it simplifies the overall anode chemistry. The cell consists of five layers; anode, anode functional layer, electrolyte, cathode layer and cathode current collection layer. They are made of nickel (Ni), nickel-yttria-stabilised zirconia (Ni-YSZ) cermet, yttria-stabilised zirconia (YSZ), yttria-stabilised zirconia-lanthanum strontium manganite (YSZ-LSM) composite, and lanthanum strontium manganite (LSM), respectively. The governing equations for gas-phase species, energy, momentum, and charge balance are coupled with kinetics equations, which describe the electrochemical reactions.

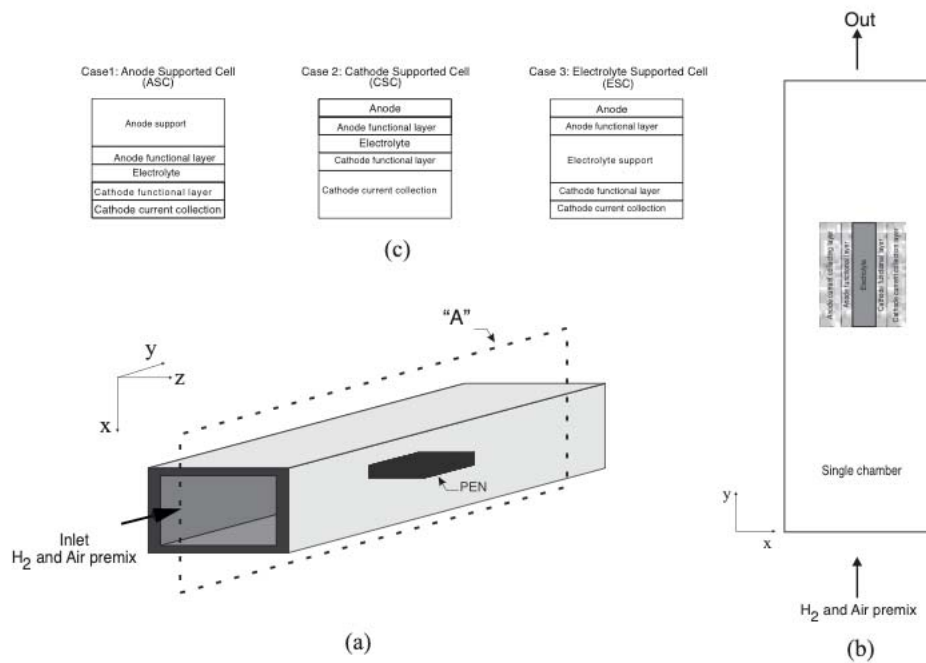


Fig. 1: (a) Schematic illustration of a 3D view of a planar SC-SOFC, (b) cross-section of a planar SC-SOFC which represents computational domain (detailed "A"), (c) schematic of different support types used for

current study (not to scale)

Three geometrical types of planar SC-SOFC were investigated here: i) anode-supported, ii) cathode-supported, and iii) electrolyte-supported. Table1 tabulates the geometrical data for our model.

Table1: Geometrical data

Description	Symbol	Value		
		Anode-supported	Cathode-supported	Electrolyte-supported
Channel length	$L_{ch}$	250 [mm]	250 [mm]	250 [mm]
Channel height	$H_{ch}$	25 [mm]	25 [mm]	25 [mm]
Cell length	$L_{cell}$	20 [mm]	20 [mm]	20 [mm]
Anode thickness	$t_a$	1000 [ $\mu\text{m}$ ]	100 [ $\mu\text{m}$ ]	100 [ $\mu\text{m}$ ]
Anode functional layer thickness	$t_{af}$	20 [ $\mu\text{m}$ ]	20 [ $\mu\text{m}$ ]	20 [ $\mu\text{m}$ ]
Electrolyte thickness	$t_e$	500 [ $\mu\text{m}$ ]	500 [ $\mu\text{m}$ ]	1000 [ $\mu\text{m}$ ]
Cathode current collector thickness	$t_c$	100 [ $\mu\text{m}$ ]	1000 [ $\mu\text{m}$ ]	100 [ $\mu\text{m}$ ]
Cathode functional layer thickness	$t_{cf}$	20 [ $\mu\text{m}$ ]	20 [ $\mu\text{m}$ ]	20 [ $\mu\text{m}$ ]

The simplifying assumptions of our study are listed in the following.

- It is assumed that the electrodes are selective. This means that the following reactions occur at the electrodes.

Anode oxidation of hydrogen:



Cathode reduction of oxygen:



- Flow is two-dimensional, compressible and laminar with Mach number lower than 0.3
- All species behave as an ideal gas.

- The electrolyte is fully impermeable.
- The inertia term in porous media flow is neglected (Stokes-Brinkman's assumption).
- The thermal diffusion is disregarded.
- The ohmic resistance due to electron transport is neglected since the electronic conductivity of the electrodes is noticeably high compared to ionic conductivity.
- The thermal equilibrium is valid between solid and fluid phases in porous electrodes.

The governing equations are described separately below.

### 2.1. Conservation of mass and momentum

The continuity equation for compressible fluids is stated as [29]

$$\frac{\partial(\varepsilon\rho)}{\partial t} + \nabla \cdot (\rho\mathbf{u}) = 0 \quad (3)$$

where  $\rho$  is the density of the mixture and  $\mathbf{u}$  is the velocity vector.  $\varepsilon$  is the porosity of the porous electrodes with a value between 0 and 1. Considering free fluid flow inside the chamber, the continuity equation is obtained by setting the porosity value to unity.

The single-phase fluid flow equation for a compressible flow in porous electrodes using Darcy's law is expressed as [30 and 31]:

$$\frac{\rho}{\varepsilon} \left( \frac{\partial \mathbf{u}}{\partial t} + (\mathbf{u} \cdot \nabla) \frac{\mathbf{u}}{\varepsilon} \right) = \nabla \cdot \left( -p\mathbf{I} + \frac{\mu}{\varepsilon} (\nabla \mathbf{u} + (\nabla \mathbf{u})^T) - \frac{2\mu}{3\varepsilon} (\nabla \cdot \mathbf{u})\mathbf{I} \right) + \rho \mathbf{g} - \left( \frac{\mu}{\kappa} \right) \mathbf{u} + \mathbf{F} \quad (4)$$

where  $\mu$  is the dynamic viscosity of the fluid,  $\varepsilon$  and  $\kappa$  are porosity and permeability of the porous electrodes, respectively, and  $\mathbf{F}$  is the volume force acting on the fluid. By applying Stokes-Brinkman's assumption the inertial term  $((\mathbf{u} \cdot \nabla) \frac{\mathbf{u}}{\varepsilon})$  in porous electrode flow vanish. In

a free media gas chamber, porosity  $\varepsilon$  is taken to be unity while, permeability  $\kappa$  is infinite.

Furthermore, as it is assumed that the electrolyte layer is impermeable, the mass and

momentum equations should not apply in this layer. The dynamic viscosity of a multicomponent mixture,  $\mu_f$ , is obtained by:

$$\mu_f = \sum_j x_j \mu_j \quad (5)$$

where  $\mu_j$  is the dynamic viscosity of the  $j$ th species of the mixture and  $x$  is its mole fraction.

## 2.2. Species conservation

The governing equation of species conservation for an individual species  $i$  can be written as [31]:

$$\varepsilon \rho \frac{\partial \omega}{\partial t} + \rho(\mathbf{u} \cdot \nabla) \omega_i = R_i \quad (6)$$

where  $\mathbf{j}_i$  is the relative mass flux vector,  $\omega_i$  is the mass fraction of the  $i$ th species, and  $R_i$  is the source term that accounts for mass deposit or mass creation of the  $i$ th species. By applying the Maxwell-Stefan diffusion model, the relative mass flux vector can be written as [32]

$$\mathbf{j}_i = -\rho \omega_i \sum_k D_{ik} \mathbf{d}_k \quad (7)$$

where  $\mathbf{d}_k$  is the diffusional driving force and  $D_{ik}$  are the multicomponent Fick's diffusivities calculated by [32]:

$$D_{ik} = 1.883 \times 10^{-2} T^{1.5} (1/M_i + 1/M_k)^{1/2} / (p \sigma_{ik}^2 \Omega_D) \quad (8)$$

where  $\sigma$  is the characteristic length in Angstrom and  $\Omega_D$  is the diffusion collision integral.

The multicomponent Fick's diffusivities are corrected to account for mass transfer resistance in the porous electrodes according to the following equation:

$$D_{ik}^{eff} = (\varepsilon/\tau) D_{ik} \quad (9)$$

where  $\tau$  is the tortuosity of porous media. In this work, the Dusty Gas Model (DGM) is applied in order to account for the impact of Knudsen diffusion in small pores. In porous electrodes, the multicomponent Fick's diffusivities in Equation (6) are then substituted with the effective DGM diffusivities which are formulated by [33]:

$$D_{DGM,ik}^{eff} = (\varepsilon/\tau)(D_{ik} \cdot D_{KN,ik}) / (D_{ik} + D_{KN,ik}) \quad (10)$$

where  $D_{KN,ik}$  are the Knudsen diffusivities which are calculated based on the free molecular flow theory [33]:

$$D_{KN,ik}^{eff} = 4/3r_p \sqrt{R_u T (M_i + M_k)} / (\pi M_i M_k) \quad (11)$$

where  $r_p$  is the effective pore radius and  $R_u$  is the universal gas constant.

As stated before, the electrolyte layer is assumed to be impermeable thus none of the species can diffuse and the species conservation equation is inactive for this layer.

### 2.3. Charge conservation

Since the characteristic time scale for charge transfer is much shorter than for heat and mass transfer [34], ionic and electronic charge conservation equations are solved in steady state [30]. By applying ohm's law, ionic and electronic charge conservation equations are stated as [34]:

$$-\nabla \cdot (\sigma_e \nabla \phi_e) = j_e \quad (12)$$

$$-\nabla \cdot (\sigma_i \nabla \phi_i) = j_i \quad (13)$$

respectively, where  $\sigma_e$  and  $\sigma_i$  are the electronic and ionic conductivity and  $\Phi_e$  and  $\Phi_i$  are the electric and ionic potential, respectively.

The right-hand sides of equations (12) and (13) describe electrical and ionic charge source/sink terms, respectively, and only exist in the anode and cathode functional layers.

According to equations (1) and (2), electrons and ions are produced in the anode and cathode catalyst layers, respectively. The electrical and ionic charge source for the anode functional layer are sink and source terms, whereas for the cathode layer they are source and sink terms, respectively. Consequently, the sink and source term of the charge conservation equation for the anode and cathode layers are stated using the Butler-Volmer equation [35-37]:

$$j_{i,a} = -j_{e,a} = A_a J_{0,ref}^{H_2} \left( c_{H_2} / c_{H_2,ref} \right)^{\gamma_{H_2}} \left[ \exp(n\alpha_a F \eta_{act,a} / R_u T) - \exp(-n(1-\alpha_a) F \eta_{act,a} / R_u T) \right] \quad (14)$$

$$j_{e,c} = -j_{i,c} = A_c J_{0,ref}^{O_2} \left( c_{O_2} / c_{O_2,ref} \right)^{\gamma_{O_2}} \left[ \exp(n\alpha_c F \eta_{act,c} / R_u T) - \exp(-n(1-\alpha_c) F \eta_{act,c} / R_u T) \right] \quad (15)$$

where  $A$  is the electrochemically active surface area per unit volume,  $J_{0,ref}^{H_2}$  and  $J_{0,ref}^{O_2}$  are reference exchange current densities, and  $\gamma_{H_2}$  and  $\gamma_{O_2}$  are the reaction order for hydrogen oxidation and oxygen reduction at reference concentrations  $c_{H_2,ref}$  and  $c_{O_2,ref}$ , respectively,  $\alpha$  is the charge transfer coefficient whose value lies between 0 and 1,  $F$  is Faraday's constant (equal to 96487 C/mol), and  $\eta_{act}$  is the activation overpotential. The indexes "a" and "c" in the above equations denote the anode and cathode sides. The anode and cathode side activation overpotentials are calculated by [16]:

$$\eta_{act,a} = \phi_e - \phi_i \quad (16)$$

$$\eta_{act,c} = \phi_e - \phi_i - V_{OC} \quad (17)$$

respectively, where  $V_{OC}$  is the open circuit voltage calculated by the Nernst equation [38]:

$$V_{OC} = 1.317 - 2.769 \times 10^{-4} T + R_u T / 2F \ln \left( p_{H_2} \cdot p_{O_2}^{1/2} / p_{H_2O} \cdot p_{ref}^{1/2} \right) \quad (18)$$

It is worth mentioning that ion transport physics is active for anode and cathode functional layers as well as the electrolyte, whilst electron transport physics is valid for both electrode functional layers and substrate/current collection layer.

## 2.4. Energy conservation

The conservation of energy for the entire domain is governed by [39]:

$$\rho C_p \frac{\partial T}{\partial t} + \nabla \cdot (\rho C_p \mathbf{u} T - k \nabla T) = Q \quad (19)$$

Where  $C_p$  is the specific heat,  $k$  is the thermal conductivity, and  $Q$  is the energy source term due to ionic transport resistance, reversible and irreversible heat generation. In order to account for the porosity of the electrodes, the effective relationship is used for specific heat capacity ( $\rho C_p$ ) and thermal conductivity ( $k$ ) by applying the thermal equilibrium between solid and fluid phases in porous electrodes [31]:

$$(\rho C_p)_{eff} = \varepsilon (\rho C_p)_f + (1 - \varepsilon) (\rho C_p)_s \quad (20)$$

$$k_{eff} = \varepsilon k_f + (1 - \varepsilon) k_s \quad (21)$$

In above equations, the indexes “ $f$ ” and “ $s$ ” denote fluid and solid phase, respectively.

Specific heat and conductivity for the fluid mixture is determined by:

$$C_{p,f} = \sum_j \omega_j C_{p,j} \quad (22)$$

$$k_f = \sum_j x_j k_j \quad (23)$$

Where  $C_{p,j}$  and  $k_j$  are the specific heat and conductivity for each gas species, respectively,  $x$  and  $\omega$  are mole and mass fraction, respectively.

## 2.5. Boundary conditions

In order to fulfill the mathematical modelling, specifying the boundary conditions for each physics was necessary. Two types of boundary conditions were used: the Dirichlet boundary

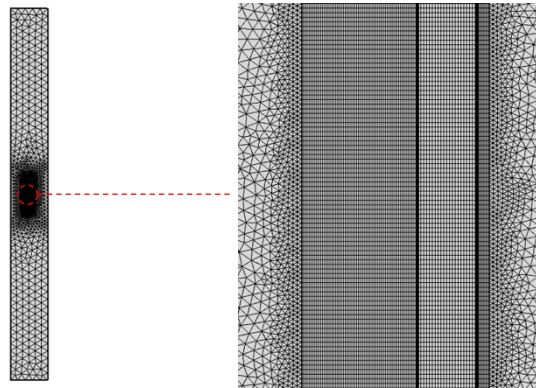
condition in which the value of the dependent variable was specified, and the Neumann boundary condition in which the derivative of the dependent variable was specified.

At the inlet of the chamber, velocity, pressure, mass fraction of species and temperature were specified. At the chamber walls no slip ( $\mathbf{u}=0$ ) and thermal insulation boundary conditions were applied for fluid flow and energy equations, respectively, and the insulation boundary condition was used for transport of species equations. At the outlet of the chamber, the pressure was equal to the total pressure and conduction heat transfer in comparison to convection heat transfer was neglected. Similarly, the diffusion term in the species transport equation was disregarded versus the convection term. At the intersection between electrodes and gas channel, the voltage was specified. In other words, the cell voltage and ground voltage were applied for cathode-channel and anode-channel intersections, respectively. Since the electrolyte was impermeable to mass and electron transport and also fluid flow, the insulation boundary condition was used for fluid flow, mass, species and electron transport equations at all exterior boundaries of the electrolyte layer. Plus, as the electrons could not diffuse to the chamber, the insulation boundary condition was applied for the electron transport equations at all intersections between electrodes and chamber, respectively. Furthermore, since it was assumed that the electrochemical reactions occur in the catalyst layers, the insulation boundary condition was utilised for the ion transportation physics at the electrodes-catalyst layer interfaces. The continuity boundary condition was applied for the rest of the boundary conditions.

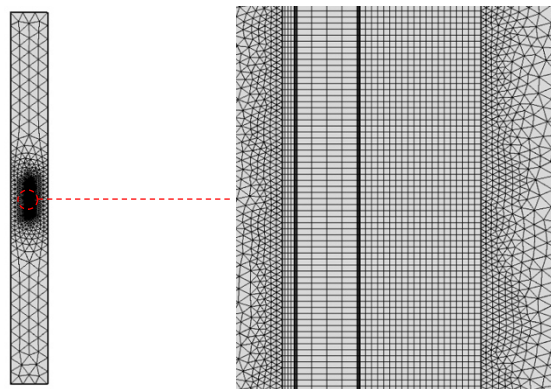
### **3. Numerical procedure**

An in-house two dimensional computational fluid dynamics (CFD) code was utilised. The code was based on the finite element method. Two types of mesh were used in order to have

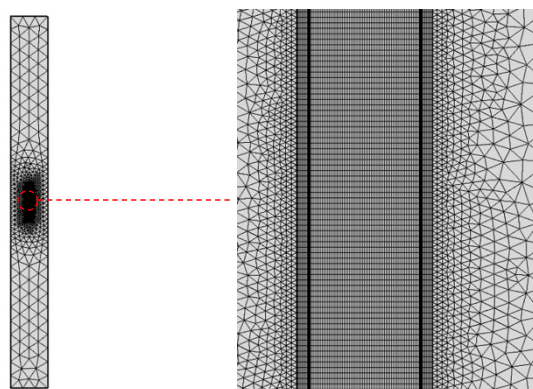
better convergence. A triangular mesh was used for the chamber and a mapped mesh used for the cell (as shown in Fig.2).



(a) AS-SOFC



(b) CS-SOFC



(c) ES-SOFC

Fig. 2: Mech structural used for current study: (a) Anode-supported SOFC (b) Cathode-

## supported SOFC (c) Electrolyte-supported SOFC

The mesh distribution was such that more elements were concentrated in the catalyst domains where more calculation volume existed.

Our study included steady state and time-dependent approaches to the problem. Table 2 tabulates the number of elements and solution time for each cell type. In the steady state study of the problem, to catch instabilities occurring in the solution procedure, the governing equations were solved in steps. Since the Butler-Volmer and fluid flow equations are non-linear equations, the ionic and electronic current distributions were obtained initially, then the fluid flow equations are solved. Finally, all governing equations were solved fully-coupled. The solution for each step was stored and applied as an initial guess for the next step. To improve the accuracy of the solution, the second-order elements for the velocity components and first order elements for the pressure field were applied in a discretisation process, while linear elements were used for the other dependent variables. The relative tolerance of  $1 \times 10^{-6}$  was chosen. The calculations were performed on a laptop with the following specifications: processor Intel (R) Core™ i7 CPUX980 @ 2.2 GHz with an installed RAM of 16 GB.

Table 2. Mesh element number and solution time obtained for each cell type.

Cell Type	Triangular elements	Quadrilateral elements	Steady state study solution time	Time-dependent study solution time
Anode supported	14600	19600	1 hr 32 min 33 s	-
Cathode supported	15811	21200	10 min 21 s	42 hr 46 min 5 s
Electrolyte supported	17658	34400	7 min 4 s	-

## 4. Results and discussion

### 4.1. Model validation

In order to show the accuracy of our model results, a validation was performed. Due to lack of experimental data in the area of SC-SOFC with hydrogen-air premix, the results were compared to experimental data provided by Rogers et al [40] for a dual chamber SOFC using hydrogen as fuel. Fig. 3 shows how our model results for a dual chamber configuration are in agreement with the experimental data. The  $R^2$  value is obtained to indicate how the current model fits the experimental data. Higher values indicate that the model fits the experimental data better. The  $R^2$  value for current model is obtained as 0.995. In order to calibrate our model results, the electrochemically active surface area per unit volume at anode and cathode and also the anodic and cathodic charge transfer coefficients were considered as fitting parameters. The current data were obtained with  $A_a=7.25616\times 10^5 \text{ m}^2/\text{m}^3$ ,  $A_c=4.0312\times 10^7 \text{ m}^2/\text{m}^3$ ,  $\alpha_a = 0.75$  and  $\alpha_c = 0.125$ . These fitting parameters were maintained for our study. The input parameters used for validation are tabulated in Table 3.

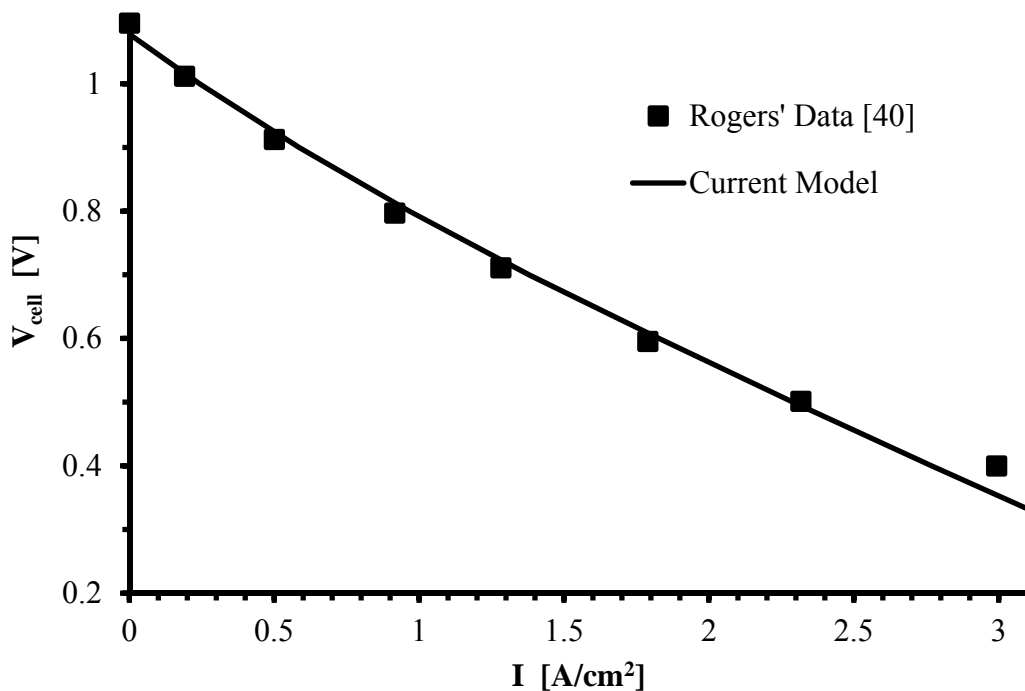


Fig. 3: The current model accuracy applied to a dual chamber configuration compared to Rogers' data.

Table 3: Input parameters used in validation.

Description	Symbol	Value	Dimensions

<i>Geometrical parameters:</i>			
Anode and cathode channel height	$H_{ch}$	0.5	mm
Anode and cathode channel width	$W_{ch}$	10	mm
Anode thickness	$t_a$	1	mm
Anode functional layer thickness	$t_{ca}$	0.02	mm
Electrolyte thickness	$t_e$	0.01	mm
Cathode layer thickness	$t_{cc}$	0.02	mm
Cathode current collector thickness	$t_c$	0.05	mm
<i>Thermo-physical parameters:</i>			
Inlet velocity	$u_{in}$	5	m/s
Inlet temperature	$T_{in}$	1073	K
Total inlet pressure	$P_{in}$	1	atm
H <sub>2</sub> inlet molar fraction	$x_{0,H_2}$	0.95	1
H <sub>2</sub> O inlet molar fraction	$x_{0,H_2O}$	0.05	1
O <sub>2</sub> inlet molar fraction	$x_{0,O_2}$	0.21	1
N <sub>2</sub> inlet molar fraction	$x_{0,N_2}$	0.79	1
Inlet velocity	$u_{in}$	5	m/s
Anode and cathode permeability [15]	$\kappa$	$10^{-13}$	m <sup>2</sup>
Anode and cathode porosity [31]	$\varepsilon$	0.375	1
Anode and cathode tortuosity [31]	$\tau$	2.75	1
Pore diameter in porous media [31]	$d_p$	0.0015	mm
Universal gas constant	$R_u$	8.314	J/mol.K
Anode thermal conductivity [15]	$k_a$	3	W/m.K
Cathode thermal conductivity [15]	$k_c$	3	W/m.K

Electrolyte thermal conductivity [15]	$k_e$	2	W/m.K
Anode conductivity [15]	$\sigma_a$	71428.57	S/m
Cathode conductivity [15]	$\sigma_c$	5376.34	S/m
Electrolyte conductivity [15]	$\sigma_e$	0.64	S/m
Anode specific heat [15]	$C_{p,a}$	595	J/kg.K
Cathode specific heat [15]	$C_{p,c}$	573	J/kg.K
Electrolyte specific heat [15]	$C_{p,e}$	606	J/kg.K
Anode density [15]	$\rho_a$	6870	kg/m <sup>3</sup>
Cathode density [15]	$\rho_c$	6570	kg/m <sup>3</sup>
Electrolyte density [15]	$\rho_e$	5900	kg/m <sup>3</sup>
Dynamic viscosity of hydrogen [15]	$\mu_{H_2}$	$6.162 \times 10^{-6} + 1.145 \times 10^{-8} \times T$	Pa.s
Dynamic viscosity of oxygen [15]	$\mu_{O_2}$	$1.668 \times 10^{-5} + 3.168 \times 10^{-8} T$	Pa.s
Dynamic viscosity of nitrogen [15]	$\mu_{N_2}$	$1.435 \times 10^{-5} + 2.642 \times 10^{-8} T$	Pa.s
Dynamic viscosity of water [15]	$\mu_{H_2O}$	$4.567 \times 10^{-6} + 2.209 \times 10^{-8} \times T$ (W/(m.K))	Pa.s
Thermal conductivity of hydrogen [15]	$k_{H_2}$	$0.08525 + 2.964 \times 10^{-4} T$	W/m.K
Thermal conductivity of oxygen [15]	$k_{O_2}$	$0.01569 + 5.69 \times 10^{-5} T$	W/m.K
Thermal conductivity of nitrogen [15]	$k_{N_2}$	$0.01258 + 5.444 \times 10^{-5} T$	W/m.K
Thermal conductivity of water [15]	$k_{H_2O}$	$-0.0143 + 9.782 \times 10^{-5} T$	W/m.K

#### 4.2. Steady-state performance analysis

In this section the steady-state and time-dependent performance of the anode, cathode and electrolyte-supported cells will be studied. The geometrical data of the different cell types considered in this study are tabulated in Table 1. All input data used in the validation stage remained constant except the inlet temperature which was equal to 773K. Also, to

ensure the safety of the system, the mixture composition was considered as 50% hydrogen, 50% air by volume. Fig. 4 depicts the i-V and i-W plots for different cells, i.e. anode-supported, electrolyte-supported, and cathode-supported cells. It can be seen that anode- and cathode-supported cells reveal better performance, however the cathode-supported cell performance is just limited to conditions close to the open circuit voltage. The maximum power density for the anode-supported cell is 43.7 mW/cm<sup>2</sup> while this value for the electrolyte-supported cell is only 22.0 mW/cm<sup>2</sup>. This low maximum power density produced by the electrolyte-supported cell is due to the higher resistance of the thicker electrolyte. It can be also seen that the cathode-supported cell reveals the same performance compared to anode-supported cell at current densities less than 0.02 A/cm<sup>2</sup>. After this point the cell does not reach to stable performance at voltages less than 0.92V.

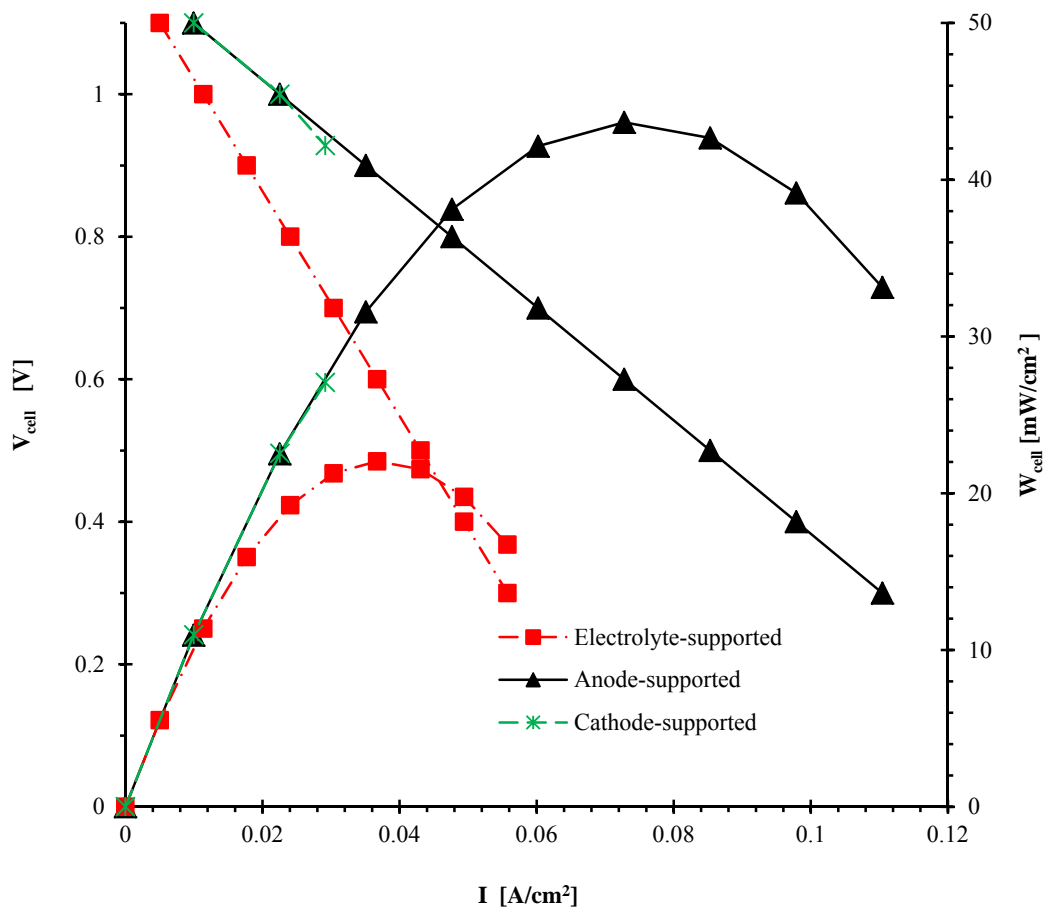


Fig. 4: i-V and i-W plots for different cell types.

Figs. 5a, 5b and 5c show oxygen concentration distribution at voltages 1.1, 1, 0.92V and inlet cell temperature 773K along a y-axis passing through the center of the cathode functional layer for cathode-supported, anode-supported and electrolyte-supported cells, respectively. It can be seen that in all cell types, the amount of oxygen inside the cathode decreases as the working cell voltage decreases. This shows that more oxygen is consumed according to equation (2) in order to provide more current. It is also found that the oxygen concentration through the cathode layer of a cathode-supported cell is lower compared to the other two cell types. This reduction in oxygen concentration continues until this value tends to zero at 0.92V. This is why the cathode-supported cell does not reach a steady-state performance at voltages less than 0.92V.

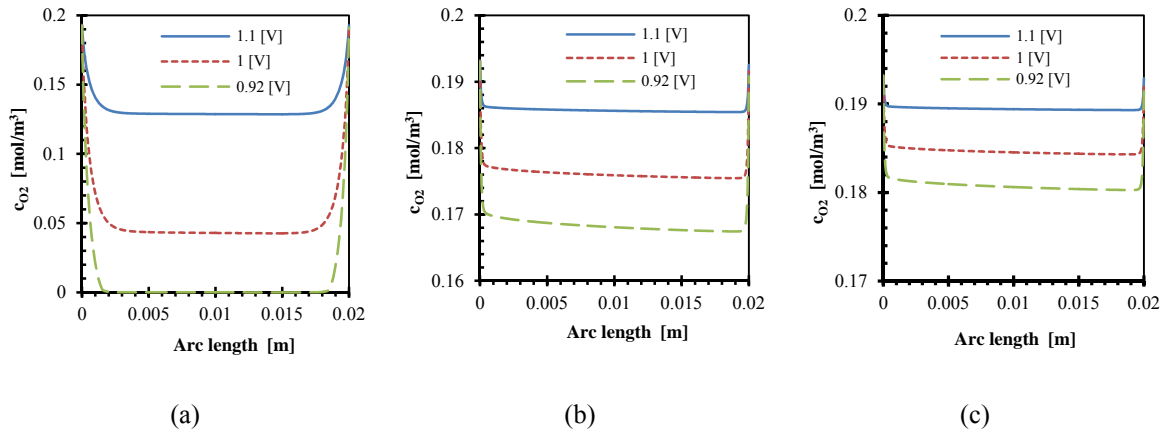


Fig. 5: Oxygen concentration distribution along a y-axis passing through the centre of the cathode functional layer at voltages 1.1, 1, 0.92V and 773K: a) cathode-supported b) anode-supported c) electrolyte-supported.

The low oxygen concentration within the cathode layer of the cathode-supported cell is related to the difficulty of oxygen diffusion from the oxygen stream inside the chamber through the relatively thick layer of cathode current collector in the presence of a lighter hydrogen molecule. However, as shown, the anode- and electrolyte- supported cells which have the same cathode functional and current collection layer thickness, reveal a

different oxygen concentration within the cathode functional layer. The minimum oxygen concentration at the cathode functional layer of the anode-supported cell is  $0.17 \text{ mol/m}^3$  at  $0.92\text{V}$  while this value for the electrolyte-supported cell is  $0.02 \text{ mol/m}^3$ . This difference is due to the better performance of the anode-supported cell compared to the electrolyte-supported cell which is clear from Fig. 3 and results in a higher amount of oxygen consumed according to equation (2).

Figs. 6a, 6b and 6c show the hydrogen concentration distribution at voltages 1.1, 1,  $0.92\text{V}$  and inlet cell temperature  $773\text{K}$  along a y-axis passing through the centre of the cathode functional layer for cathode-supported, anode-supported and electrolyte-supported cells, respectively. It is clear that hydrogen can more easily diffuse to the functional layer of the cathode-supported cell compared to the other two cells. Consequently, the hydrogen which is not participating in the cathodic electrochemical reaction is accumulated. The maximum of hydrogen concentration in this case reaches  $15.22 \text{ mol/m}^3$  while this value for anode- and electrolyte- supported cells is  $14.77$  and  $14.74 \text{ mol/m}^3$ , respectively.

Figs. 7a, 7b and 7c show the water concentration distribution at voltages 1.1, 1,  $0.92\text{V}$  and inlet cell temperature  $773\text{K}$  along a y-axis passing through the centre of the cathode functional layer for cathode-supported, anode-supported and electrolyte-supported cells, respectively. A slight accumulation of water is observed in all cells, however, the amount of water accumulation for the cathode-supported cell is about 10% greater than the value for anode- and electrolyte-supported cells.

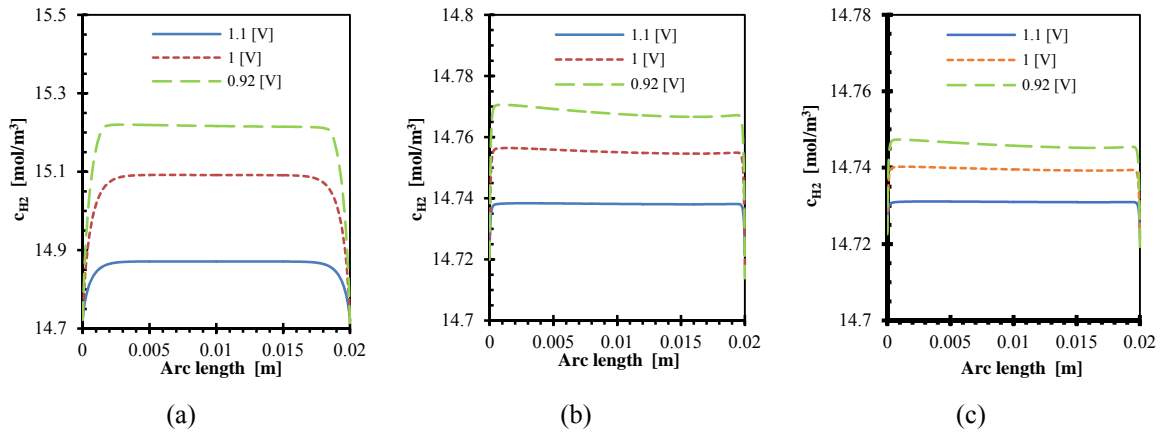


Fig. 6: Hydrogen concentration distribution along a y-axis passing through the centre of the cathode functional layer at voltages 1.1, 1, 0.92V and 773K: a) cathode-supported b) anode-supported c) electrolyte-supported.

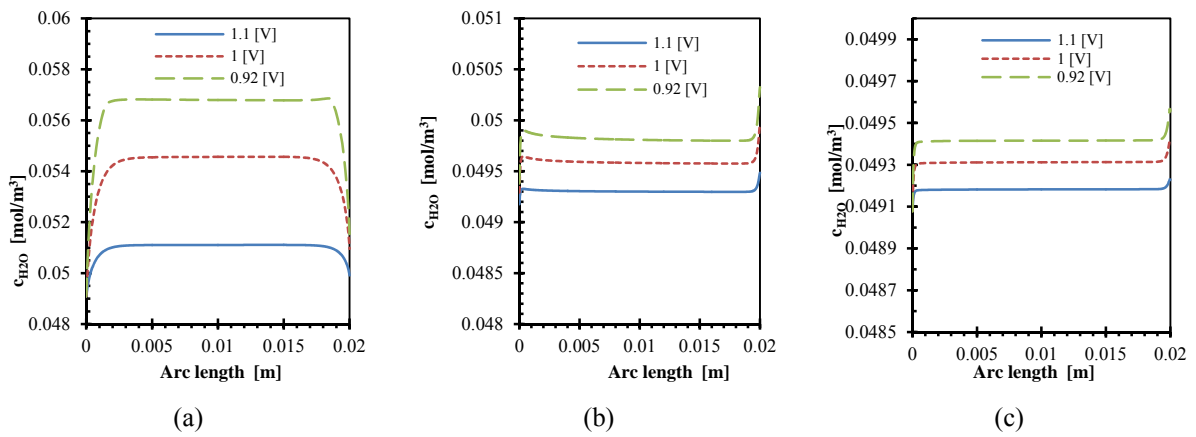


Fig. 7: Water concentration distribution along a y-axis passing through the center of the cathode functional layer at voltages 1.1, 1, 0.92V and 773K: a) cathode-supported b) anode-supported c) electrolyte-supported

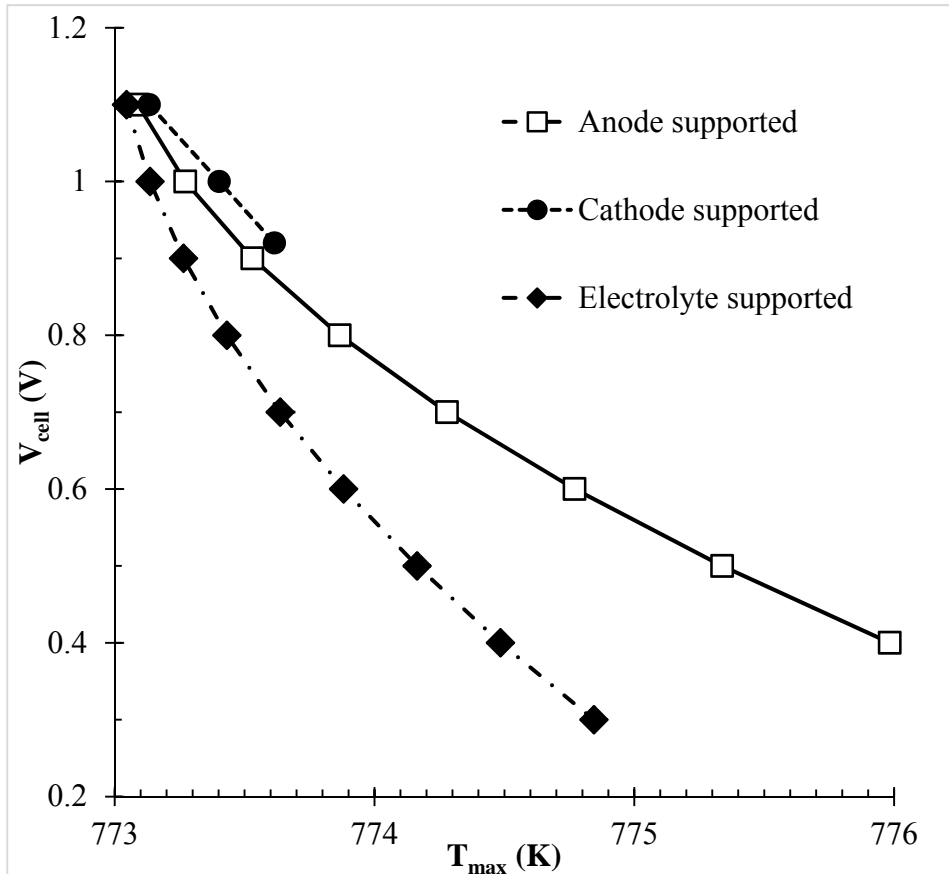


Fig. 8: Maximum cell temperature distribution for each support types

Fig. 8 represents maximum cell temperature in each cell voltages for different support types considered in this study. As expected, maximum cell temperature increases with decreasing of cell voltage for all support types. This is due to more losses occur in lower cell voltages. The changes in maximum cell temperature for both anode- and cathode-supported cell are the same. However, anode-supported cell reveals more temperature gradient compare to electrolyte-supported cell. For electrolyte-supported cell, the maximum cell temperature value is about 774.5K at cell voltage 0.4V while this value for anode-supported cell is 776K at the same working condition.

#### 4.3. Time-dependent performance analysis

In this section the cell response to a negative step change in working voltage from 1V to 0.9V is investigated. As the steady-state performance study in section 4.2 showed that the cathode-supported cell does not reach to its steady-state performance at voltages less than 0.92V, this specific negative step change was chosen. Fig. 9 shows the negative step change in working voltage applied to the cathode-supported cell. This sudden change in voltage was introduced at  $t=3s$ . Steady-state simulation results at 1V served as an initial solution for the time dependent study. Since the steady-state study of the cells revealed a slight temperature gradient within the cell, the energy equation was not solved in the time dependent study and all temperature gradients obtained in the steady-state study stage were retained to save computing time.

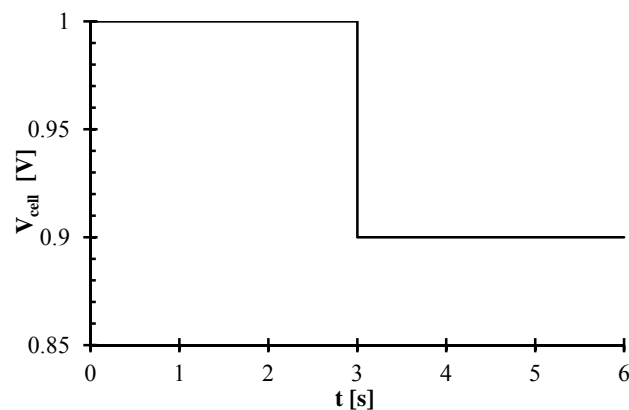


Fig. 9: The negative step change in working voltage applied to cells from 1V to 0.9V.

Fig. 10 depicts the current density response of the cathode-supported cell to a negative step change in voltage from 1 to 0.9V at  $t=3s$ . The plot shows an initial jump in current density from 0.022 to 0.035  $A/cm^2$ . This value remains constant for only about 20ms after the step change

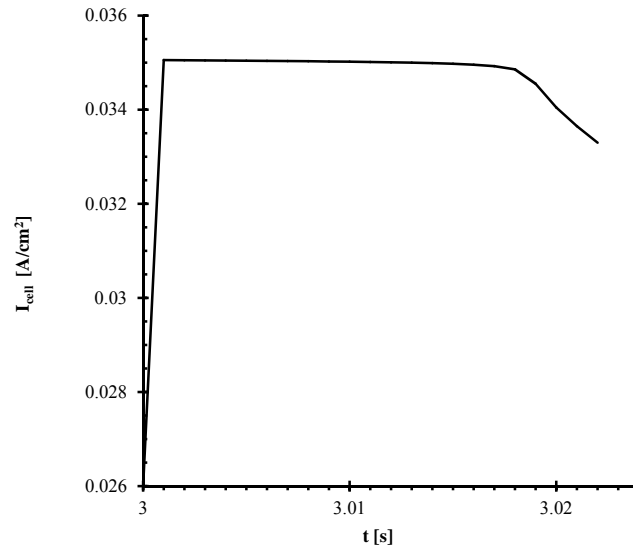


Fig. 10: Current density response of the cathode-supported cell to a negative step change in voltage from 1 to 0.9V at  $t = 3$  s .

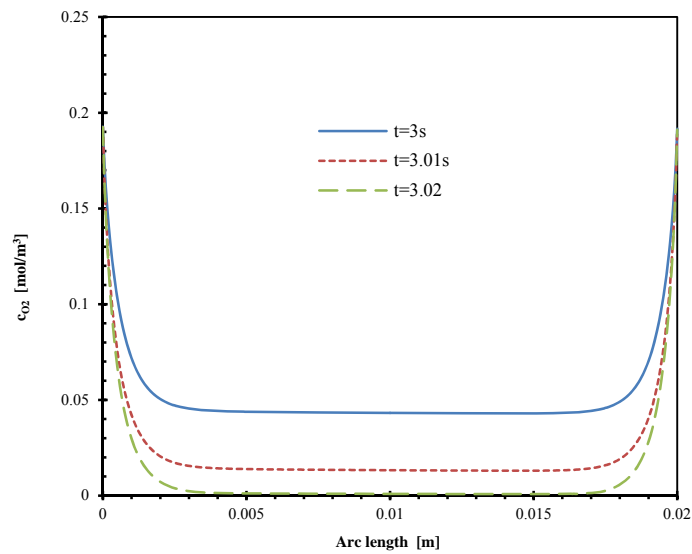


Fig. 11: Oxygen concentration distribution along a y-axis passing through the centre of the cathode functional layer as the response of the cathode-supported cell to a negative step change in voltage from 1 to 0.9V at  $t = 3$  s .

in voltage is introduced. After that the current density decreases. By plotting the oxygen distribution along a y-axis passing through the centre of the cathode functional layer, the

response of the cathode-supported cell to this step change in Fig. 11, it was found that this reduction in current density value occurring after 20ms is due to the consumption of all oxygen present at the cathode layer.

## **5. Conclusion**

The numerical investigation of a planar single chamber solid oxide fuel cell with a focus on the support types has been reported. The steady-state study of the cells revealed the better performance of the anode-supported cell compared to the electrolyte-supported cell where the maximum power density produced by the anode-supported cell was about double of the maximum power density generated by electrolyte-supported cell. This was due to the ohmic losses which are proportional to the electrolyte thickness. Also, the cathode-supported cell showed a similar performance to the anode-supported cell at voltages above 0.92V but after that the cell did not achieve steady-state performance due to lack of oxygen at the cathode layer. Our transient performance study on the cathode-supported cell showed that the amount of oxygen at the cathode layer was consumed within 20ms after introducing the negative voltage step from 1 to 0.9V.

## References

- [1] EG and G Technical Services, Inc. Science Applications International Corporation, Fuel Cell Handbook, sixth edition, US Department of Energy, 2002.
- [2] Kamvar M., Ghassemi M., Rezaei M., Effect of catalyst layer configuration on single chamber solid oxide fuel cell performance, Journal of Applied Thermal Engineering, Vol. 100, pp.98-104, (2016), doi: 10.1016/j.applthermaleng.2016.01.128.
- [3] Kupecki J., Motylinski K., Zurawska A., Kosiorek M., Ajdys L., Numerical analysis of an SOFC stack under loss of oxidant related fault conditions using a dynamic non-adiabatic model, Int. J. Hydrogen Energy, Vol. 44, pp. 21148-21161, (2019), doi: 10.1016/j.ijhydene.2019.04.029.
- [4] El-Hay E.A., El-Hameed M.A., El-Fergany A.A., Optimized Parameters of SOFC for steady state and transient simulations using interior search algorithm, J. Energy, Vol. 166, pp. 451-461, (2018), doi: 10.1016/j.energy.Energy.2018.10.038.
- [5] Moreno-Blanco J., Elizalde-Blancas F., Riesco-Avila J.M., Belman-Flores J.M., Gallego-Munoz A., On the effect of gas channels-electrode interface area on SOFCs performance, Int. J. Hydrogen Energy, Vol. 44, pp. 446-456, (2019), doi: 10.1016/j.ijhydene.2018.02.108.
- [6] Amiri A., Tang S., Steinberger-Wilckens R., Tadé M.O., Evaluation of Fuel Diversity in Solid Oxide Fuel Cell Systems, Int. J. Hydrogen Energy, Vol. 43, pp. 23475-23487 (2018).
- [7] Bove R. , Ubertini S., Modeling Solid Oxide Fuel Cells, Methods, Procedures and Technologies, 1<sup>st</sup> ed. Springer, (2008).

- [8] Wang Y., Jiang W., Luo Y., Zhang Y., Tu Sh., Evolution of thermal stress and failure probability during reduction and re-oxidation of solid oxide fuel cell, *J. Power Sources*, Vol. 371, pp. 65-76, (2017), doi: [10.1016/j.jpowsour.2017.10.034](https://doi.org/10.1016/j.jpowsour.2017.10.034).
- [9] Chaudhary Tariq N., Umer S., Baixin Ch., Reacting flow coupling with thermal impacts in a single solid oxide fuel cell, *Int. J. Hydrogen Energy*, Vol. 44, pp. 8425-8438, (2019), doi: [10.1016/j.ijhydene.2019.02.043](https://doi.org/10.1016/j.ijhydene.2019.02.043).
- [10] Hao Y., Shao Z., Mederos J., Lai W., Goodwin D.G., Haile S.M., Recent advances in single-chamber fuel cells: Experiment and modeling, *Solid State Ionics*, Vol. 177, pp. 2013-2021, (2006), doi:[10.1016/j.ssi.2006.05.008](https://doi.org/10.1016/j.ssi.2006.05.008).
- [11] Ahn S., Kim Y., Moon J., Lee J., Kim J., Influence of patterned electrode geometry on performance of co-planar, single-chamber, solid oxide fuel cell, *J. Power Sources*, Vol. 171, pp. 511-516, (2007), doi:[10.1016/j.jpowsour.2007.06.025](https://doi.org/10.1016/j.jpowsour.2007.06.025).
- [12] Yano M., Tomita A., Sano M., Hibino T., Recent advances in single-chamber solid oxide fuel cells: A review, *Solid State Ionics*, Vol. 177, pp. 3351-3359, (2007), doi:[10.1016/j.ssi.2006.10.014](https://doi.org/10.1016/j.ssi.2006.10.014).
- [13] Akhtar N., *Single-Chamber Solid Oxide Fuel Cells: Modeling and Experiments*, PhD thesis, University of Birmingham (2010).
- [14] Chung Ch.Y., Chung Y.Ch., Performance characteristics of micro single-chamber solid oxide fuel cell: Computational analysis, *J. Power Sources*, Vol. 154, pp. 35-41, (2006), doi:[10.1016/j.jpowsour.2005.03.229](https://doi.org/10.1016/j.jpowsour.2005.03.229).
- [15] Akhtar N., Decent S.P, Kendall K., Numerical modeling of methane-powered micro-tubular, single-chamber solid oxide fuel cell, *J. Power Sources*, Vol. 195, pp. 7796-7807, (2010), doi: [10.1016/j.jpowsour.2010.01.084](https://doi.org/10.1016/j.jpowsour.2010.01.084).

- [16] Akhtar N., Decent S.P., Loghin D., Kendall K., A three dimensional numerical model of a single-chamber solid oxide fuel cell, *Int. J. Hydrogen Energy*, Vol. 34, pp. 8645-8663, (2009), [doi:10.1016/j.ijhydene.2009.07.113](https://doi.org/10.1016/j.ijhydene.2009.07.113).
- [17] Akhtar N., Decent S.P., Kendall K., A parametric analysis of a micro-tubular, single-chamber solid oxide fuel cell (MT-SC-SOFC), *Int. J. Hydrogen Energy*, Vol. 36, pp. 765-772, (2011), [doi:10.1016/j.ijhydene.2010.10.032](https://doi.org/10.1016/j.ijhydene.2010.10.032).
- [18] Jacques-Bedrad X., Napporn T.W., Roberge R., Meunier M., Performance and ageing of an anode-supported SOFC operated in single-chamber conditions, *J. Power Sources*, Vol. 153, pp. 108-113, (2006), [doi:10.1016/j.jpowsour.2005.03.138](https://doi.org/10.1016/j.jpowsour.2005.03.138).
- [19] Morel B., Roberge R., Savoie S., Napporn T.W., Meunier M., Temperature and performance variations along single chamber solid oxide fuel cells, *J. Power Sources*, Vol. 186, pp. 89-95, (2009), [doi:10.1016/j.jpowsour.2008.09.087](https://doi.org/10.1016/j.jpowsour.2008.09.087).
- [20] Hao Y., Goodwin D.G., Numerical Modeling of Single-Chamber SOFCs with Hydrocarbon Fuels, *J. Electrochem. Soc.*, Vol. 154 (2), pp. B207-B217, (2007), doi: 10.1149/1.2404895
- [21] Akhtar N., Kendall K., Micro-tubular, solid oxide fuel cell stack operated under single-chamber conditions, *Int. J. Hydrogen Energy*, Vol. 36, pp. 13083-13088, (2011), [doi:10.1016/j.ijhydene.2011.07.057](https://doi.org/10.1016/j.ijhydene.2011.07.057).
- [22] Akhtar N., Micro-tubular, single-chamber solid oxide fuel cell (MT-SC-SOFC) stacks: Model development, *Chemical Engineering Research and Design*, Vol. 90, pp. 814-824, (2012), [doi:10.1016/j.cherd.2011.09.013](https://doi.org/10.1016/j.cherd.2011.09.013).

- [23] Akhtar N., Modeling of novel porous inserted micro-tubular, single-chamber solid oxide fuel cells (MT-SC-SOFC), *Chemical Engineering Journal*, Vol. 179, pp. 277-284 (2012), [doi:10.1016/j.cej.2011.11.001](https://doi.org/10.1016/j.cej.2011.11.001).
- [24] Hao Y., Goodwin D.G., Efficiency and fuel utilization of methane-powered single-chamber solid oxide fuel cells, *J. Power Sources*, Vol. 183, pp. 157-163, (2008), doi: 10.1016/j.jpowsour.2008.04.072.
- [25] H. Xu, B. Chen, P. Tan, J. Xuan, M. Mercedes, et al., Modelling of all-porous solid oxide fuel cells with a focus on the electrolyte porosity design, *Applied Energy*, Vol. 235, pp. 602-611 (2019), [doi:10.1016/j.apenergy.2018.10.069](https://doi.org/10.1016/j.apenergy.2018.10.069).
- [26] Kong W., Han Zh., Lu S., Gao X., Wang X., A novel interconnector design of SOFC, *Int. J. Hydrogen Energy* (In Press) (2019). doi:10.1016/j.ijhydene.2019.04.029
- [27] Schluckner C., Subotic V., Preibl S., Hochenauer C., Numerical analysis of flow configurations and electrical contact positions in SOFC single cell and their impact on local effects, *Int. J. Hydrogen Energy*, Vol. 44, pp. 1877-1895, (2019), doi: 10.1016/j.ijhydene.2018.11.132.
- [28] Moreno-Blanco J., Elizalde-Blancas F., Riesco-Avila J.M., Belman-Flores J.M., Gallegos-Munoz A., On the effect of gas channels-electrode interface area on SOFCs performance, *Int. J. Hydrogen Energy*, Vol. 44, pp. 446-456, (2019), doi: 10.1016/j.ijhydene.2018.02.108.
- [29] B.R. Munson, A.P. Rothmayer, Th.H. Okiishi, W.W. Huebsch, *Fundamental of Fluid Mechanics*, Wiley 7<sup>th</sup> ed. (2012).
- [30] G.K. Batchelor, *An Introduction To Fluid Dynamics*, Cambridge University Press, 2000.
- [31] D.A. Nield and A. Bejan, *Convection in Porous Media*, Springer, 3<sup>rd</sup> edition, 2006.
- [32] R. Taylor and R. Krishna, *Multicomponent mass transfer*, 1th ed., John Willey & Sons, Inc. (1993).

- [33] M. Andersson, J. Yuan and B. Sunden, SOFC modeling considering electrochemical reactions at the active three phase boundaries, *Int. J. Heat and Mass Transfer* 55 773-788 (2012) [doi:10.1016/j.ijheatmasstransfer.2011.10.032](https://doi.org/10.1016/j.ijheatmasstransfer.2011.10.032).
- [34] M.F. Serincan, U. Pasaogullari and N.M. Sammes, A transient analysis of a micro-tubular solid oxide fuel cell (SOFC), *J. Power Sources*, Vol. 194, pp. 864-872, (2009). [doi:10.1016/j.jpowsour.2009.06.036](https://doi.org/10.1016/j.jpowsour.2009.06.036).
- [35] M.M. Hussain, X. Li, I. Dincer, Mathematical modeling of planar solid oxide fuel cells, *J. Power Sources*, Vol. 161, pp. 1012-1022, (2006), [doi:10.1016/j.jpowsour.2006.05.055](https://doi.org/10.1016/j.jpowsour.2006.05.055).
- [36] V.M. Janardhanan and O. Deutschmann, CFD analysis of a solid oxide fuel cell with internal reforming: Coupled interactions of transport, heterogeneous catalysis and electrochemical processes, *J. Power Sources*, Vol. 162, pp. 1192-1202, (2006), [doi:10.1016/j.jpowsour.2006.08.017](https://doi.org/10.1016/j.jpowsour.2006.08.017).
- [37] H. Zhu, R.J. Kee, V.M. Janardhanan, O. Deutschmann and D.G. Goodwin, Modeling elementary heterogeneous chemistry and electrochemistry in Solid-Oxide Fuel Cells, *J. Electrochemical Society*, Vol. 152, pp. A2427-A2440, (2005), [doi: 10.1149/1.2116607](https://doi.org/10.1149/1.2116607).
- [38] D.H. Jeon, A comprehensive CFD model of anode-supported solid oxide fuel cells, *Electrochimica Acta*, Vol. 54, pp. 2727-2736, 2009, [doi: 10.1016/j.electacta.2008.11.048](https://doi.org/10.1016/j.electacta.2008.11.048).
- [35] M. Kaviany, *Principles of heat transfer in porous media*, Springer, second ed. (1995).
- [39] W.A. Rogers, R.S. Gemmen, C. Johnson, M. Prinkey, M. Shahnam, Validation and application of a CFD-based model for solid oxide fuel cells and stacks, *Fuel Cell Science Engineering Technology ASME*, Vol. 1761, pp. 517-520, (2003). [doi: 10.1115/FUELCELL2003-1762](https://doi.org/10.1115/FUELCELL2003-1762).